Bulletin of the Seismological Society of America, Vol. 92, No. 4, pp. 1154–1170, May 2002

The 1999 M_w 7.1 Hector Mine, California, Earthquake Sequence: Complex Conjugate Strike-Slip Faulting

by Egill Hauksson, Lucile M. Jones, and Kate Hutton

Abstract The 1999 M_w 7.1 Hector Mine mainshock showed right-lateral strike-slip faulting, with an initial strike of N6°W and vertical dip. The mainshock was preceded within 20 hours by 18 recorded foreshocks of $1.5 \leq M \leq 3.8$ within a few kilometers distance of the mainshock hypocenter. The aftershocks delineate how the Hector Mine earthquake ruptured with strike N6°W to the south for a distance of 15 km, and possibly to the north for a distance of several kilometers. The two largest aftershocks of M 5.9 and M 5.7 occurred near the north and south ends of the first mainshock rupture segment. The second segment of rupture, starting 15 km to the south away from the mainshock hypocenter, delineated by strike-slip and thrust-faulting aftershocks, extends 10 km farther away with a strike of S140°E along the Bullion fault. The aftershocks also outline an unusual third rupture segment, extending from about 5 km south of the hypocenter with a strike of N30°W to N35°W for a distance of 20 km. Approximately 10 to 25 km farther to the north and west of the mainshock epicenter, several clusters form a complex aftershock distribution. Three-dimensional Vp and Vp/Vs models of the region exhibit only small regional changes, as is typical for the Mojave region. Nonetheless, the mainshock rupture started within a region of rapidly varying Vp, and at least three regions of low Vp/Vs are imaged within the aftershock zone. The rate of decay for the Hector Mine earthquake sequence has been slightly above the mean for both p-values and b-values in southern California. The focal mechanisms of the aftershocks and the state of stress are consistent with strike-slip faulting, including a component of normal faulting most prominent to the north. The orientation of the regional maximum horizontal stress, the variation in orientation of the mainshock fault segments by 30°, and scattered distribution of aftershocks suggest that the mainshock and aftershock deformation field exhibit volumetric shear deformation accommodated by complex conjugate sets of strike-slip faults.

Introduction

The 1999 Hector Mine earthquake sequence occurred near the eastern edge of the eastern California shear zone (ECSZ), an 80-km-wide, more than 400-km-long zone of deformation that cuts across southern California (Dokka and Travis, 1990a). This zone extends into the Owens Valley and Death Valley regions and may accommodate as much as 12 mm/yr of the plate motion between the Pacific and North American Plates (Sauber *et al.*, 1994). Previously, the 1947 M 6.5 Manix earthquake occurred approximately 50 km north of the Hector Mine earthquake (Fig. 1; Doser, 1990). In contrast, during the 1990s, three earthquakes of $M > 6$ have occurred near the southernmost extent of the ECSZ. These earthquake sequences illuminate the slip transfer zone between the ECSZ and the San Andreas fault to the south.

The 1992 Landers sequence began with the M_w 6.1 April 1992 Joshua Tree sequence and a migration of seismicity to the north. This seismicity culminated in the occurrence of the 28 June M_w 7.3 Landers earthquake, which was followed within 3 hours by the M_w 6.3 Big Bear aftershock (Hauksson *et al.*, 1993). The October 1999 Hector Mine mainshock occurred within 8 years of the June 1992 M_w 7.3 Landers earthquake. The epicentral distance between the two events is about 50 km, and the closest points between the two ruptures are about 20 km apart (Fig. 1). These two rupture zones are in an en echelon relationship within the ECSZ, with a 50% overlap in the ruptures. Both the temporal and spatial proximity suggest that these two events are related. Parsons and Dreger (2000) speculated that the Landers mainshock somehow triggered the Hector Mine earthquake through elastic stress transfer. Alternatively, Deng *et al.* (1998) showed that the region is characterized by rapid postseismic deformation rates, and thus viscous flow in the

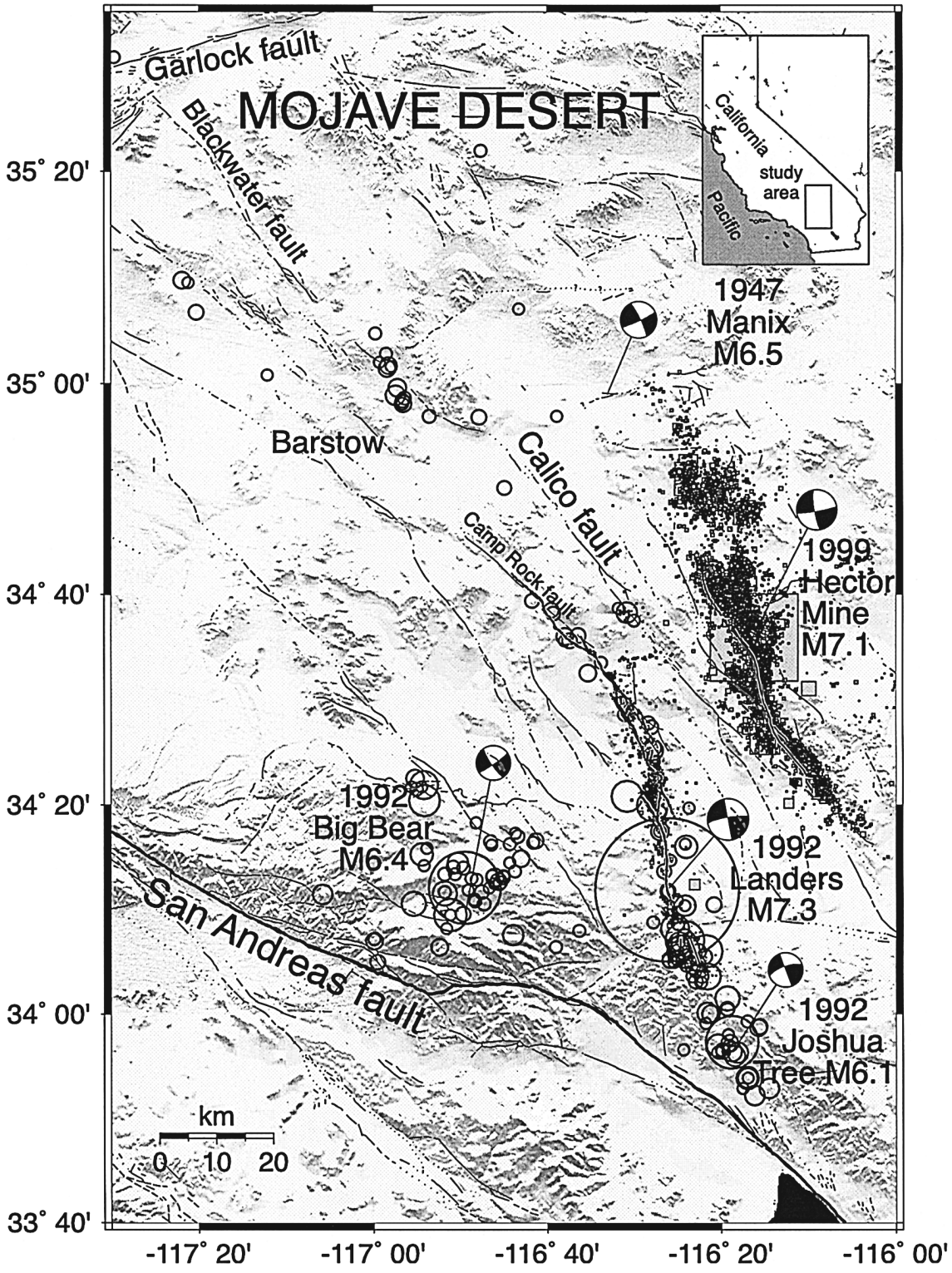

Figure 1. Overview map of the Hector Mine earthquake sequence (squares), including $M \geq 4.0$ 1992 Landers aftershocks (circles), focal mechanisms of the $M > 6$ earthquakes that have occurred in the region since 1947, the 1947 Manix, and the 1922 Joshua Tree, Landers, and Big Bear earthquakes. Both the surface ruptures of the 1992 M_w 7.3 Landers and the 1999 M_w 7.1 Hector Mine earthquakes are shown as line segments drawn on white background. Late Quaternary faults from Jennings (1994) and the Hector Mine surface rupture from Treiman *et al.* (2002).

lower crust and upper mantle may have contributed to the occurrence of the Hector Mine earthquake.

Although the Landers and Hector Mine earthquakes occurred in the same geographic region, their detailed rupture behaviors and aftershock distributions are significantly different. The Landers mainshock ruptured from south to north, jumping across fault steps as large as 5 km (Hauksson *et al.*, 1993; Sieh *et al.*, 1993). The Hector Mine earthquake ruptured from north to south along at least three different, contiguous fault segments (Ji *et al.*, 2002; Treiman *et al.*, 2002). The spatial distribution of aftershocks to the Hector Mine earthquake is more diffuse than that of the Landers event, and the focal mechanisms of the aftershocks are more diverse. In part, these features may be influenced by the network of existing faults, the crustal strength profile, the background regional stress, and possible influence of past large earthquakes in the ECSZ.

We synthesize and interpret the seismological observations from the 1999 M_w 7.1 Hector Mine earthquake sequence, including occurrence of the foreshock sequence, spatial and temporal distribution of aftershocks, and the state of stress inferred from focal mechanisms. We determine 3D Vp and Vp/Vs models and use these models in a 5-km horizontal and 4-km vertical grid to relocate the sequence. We also use these models to calculate refined first-motion focal mechanisms and use stress inversion methods to invert for the state of stress and style of faulting from the focal mechanisms.

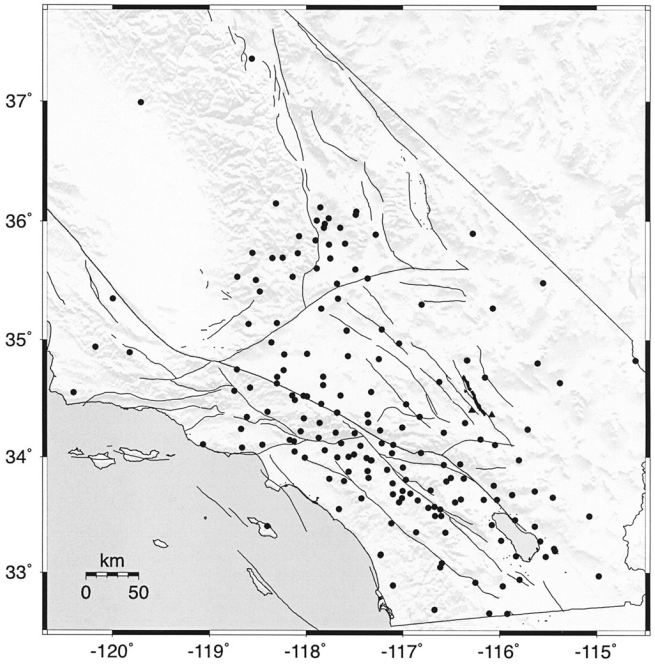

Figure 2. Seismic stations in the Southern California Seismic Network (SCSN/TriNet) that recorded data used in this study. The two stations shown as triangles were installed about 2 weeks after the occurrence of the mainshock. Surface rupture for the M_w 7.1 Hector Mine earthquake is also shown (Treiman *et al.*, 2002).

Data and Methods

The *P* and *S* arrival-time data used in this study were recorded by the Southern California Seismic Network, operated by the U.S. Geological Survey and the California Institute of Technology (SCSN/TriNet) (Fig. 2). The SCSN/TriNet has recorded more than 16,000 Hector Mine aftershocks through December 2000. All of these events have been processed by SCSN and are included in this study.

Using the coarse 40-km grid model from Hauksson (2000) we interpolate for a 5-km horizontal grid and determine 3D Vp and Vp/Vs models for the general vicinity of the Hector Mine and Landers earthquakes. We use the inversion method of Thurber (1993) and the detailed approach described in Hauksson (2000). These models are used to relocate the seismicity in the area of the Hector Mine earthquake sequence from 1981 through December 2000. The Vp and Vp/Vs models include both the 1992 Landers and the 1999 Hector Mine aftershock zones and thus have ample data to constrain the models.

The Hector Mine sequence occurred near the eastern edge of the SCSN, with the closest station located 26 km away from the mainshock and had less dense station coverage than was available for the 1992 Landers sequence (Fig. 2); however, because the velocity structure of the region is fairly uniform, the focal depths and mechanisms are quite stable. The northern part of the sequence is better constrained in depth because the closest station is located at the northern edge of the aftershock zone. About two weeks into the sequence, two more short-period stations were added to the SCSN; these improve the determination of focal depths located towards the center and to the southern part of the aftershock zone. To test the stability of the depth determination, we assign a starting depth of 8 km for all the events and show that the overall depth distribution did not change significantly. The final depths are determined by using the SCSN/TriNet depths as starting depths. Shallow aftershocks with depths of less than 2 to 4 km, however, do not have well-constrained depths. During the final relocations, the 3D Vp and Vp/Vs models were allowed to vary, using strong damping. These model perturbations absorbed about 20% of the remaining root-mean-square travel-time residuals.

We use the grid-searching algorithm and computer programs by Reasenberg and Oppenheimer (1985) to determine more than 1400 first-motion, lower-hemisphere focal mechanisms. We included background seismicity, foreshocks, mainshock, and aftershocks with 12 or more first motions. The foreshocks, mainshock and $M \geq 4.5$ aftershocks are shown in Figure 3. In most cases, the first-motion focal mechanisms are well constrained, although the median uncertainties in strike, dip, and rake of the focal mechanisms are 30°, 40°, and 60°, respectively, for the whole data set. We use the methods of Michael (1984) to determine the state of stress, using first-motion focal mechanisms from the

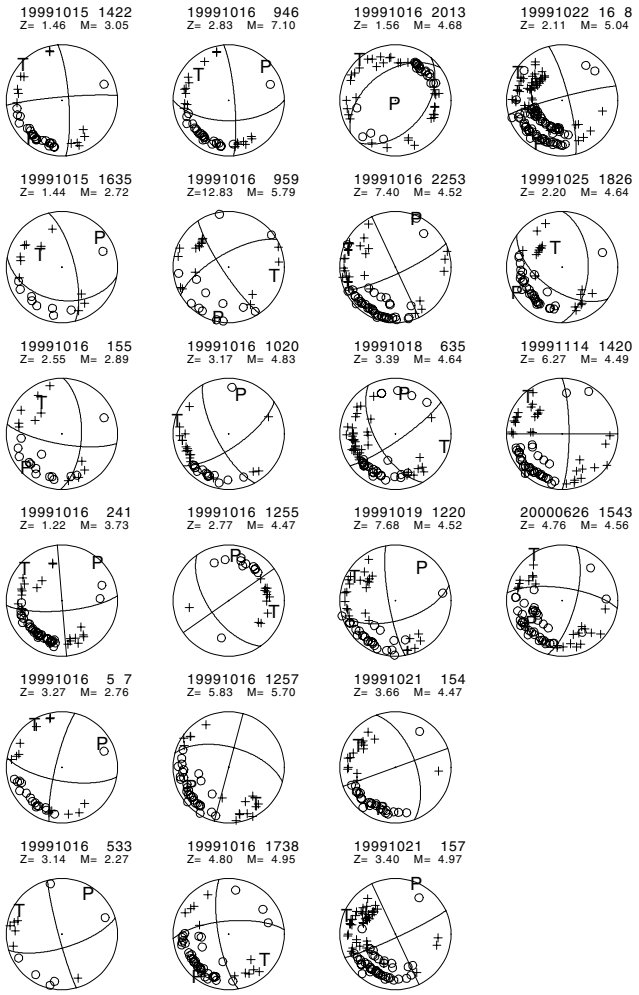

Figure 3. The first-motion focal mechanisms for selected earthquakes in the Hector Mine sequence, including the six largest foreshocks, mainshock, and the $M \geq 4.5$ aftershocks that had more than 12 first motions available.

background seismicity (1992–1999), the foreshocks, and the aftershocks.

Results

Premainshock Seismicity

Before the Landers earthquake, the SCSN did not record any significant seismicity within 5 to 10 km distance of the future epicenter of the Hector Mine earthquake. In contrast, the 1992 M_w 7.3 Landers earthquake triggered a cluster of earthquakes near the future Hector Mine hypocenter (Fig. 4). These events occurred in two distinct temporal clusters (Fig. 5a). The first started on 28 June 1992, with the largest earthquake of M 5.4, and ended in early 1994. It was located 3 km west of the Hector Mine earthquake, with a northwest trend. The largest event had a focal mechanism with oblique-thrust faulting. The second cluster lasted from August 1996 to January 1997, with the largest earthquake of M 4.3 (Fig. 5a). It was located east of the later-mapped Lavic Lake fault, in a tight 1-km-wide cluster, 1 km west of the Hector Mine mainshock (Fig. 4a). The frequency of events within the two clusters decayed with time, showing normal aftershock behavior after starting with the largest event. Earthquakes in both clusters had a mixture of dip-slip (primarily reverse) and strike-slip mechanisms, often including one nodal plane subparallel to the future rupture along the Lavic Lake fault (Hauksson *et al.*, 1993). Both clusters had several microearthquakes recorded within 0.5 km of the future hypocenter of the M_w 7.1 Hector Mine earthquake, although most of these were located at the north edge of the cluster of immediate Hector Mine foreshocks.

The aftershocks following the M_w 7.1 Hector Mine mainshock that were located in the immediate vicinity of the mainshock hypocenter were mostly separated in space from the premainshock seismicity (Fig. 4b). These aftershocks were predominantly located east of the Lavic Lake fault, well east of the earlier cluster. The aftershocks surround a zone of relative quiescence that coincided with the region of the 1996 swarm. Thus, the Hector Mine sequence does not spatially coincide with the previous background seismicity in the region. This overall pattern of seismicity suggests that the premainshock seismicity, the mainshock, and aftershocks released tectonic strains within adjacent crustal volumes, extending progressively farther to the east, into regions of decreasing tectonic strain rate (Sauber *et al.*, 1994).

Foreshocks and Mainshock

A total of 18 foreshocks were recorded preceding the Hector Mine mainshock, starting about 19 hours before the mainshock, with the largest foreshock of M_L 3.7 occurring 7 hours before the mainshock (Fig. 5b). These foreshocks formed a cluster within 1 km epicentral distance of the hypocenter of the mainshock (Fig. 4a). This cluster was elongated north-south about 0.5 km, which is similar to the general relocation accuracy using the new 3D Vp and Vp/Vs models for this region of about 0.5 km. The foreshocks showed mostly strike-slip mechanisms similar to the mainshock, although these are in some cases not as well constrained (Fig. 3).

The mainshock that occurred at 9h46m UTC on 16 October 1999 had a moment magnitude of M_w 7.1 (Scientists of the USGS *et al.*, 2000) and was located 48 km north of Joshua Tree. It was felt throughout southern California, but caused only minor damage in the remote desert areas. The seismic moment of the mainshock was 6.28×10^{19} Nm with an average stress drop of 25 bars (Ji *et al.*, 2002). The mainshock hypocentral depth was 5 ± 4 km, which has such large error because the nearest station is 26 km away. The mainshock hypocenter is located 2 km east of the main trace of the later mapped Lavic Lake fault, which strikes N35°W. In the immediate vicinity of the mainshock epicenter, Treiman *et al.* (2002) mapped a 200- to 300-m-wide zone of surface breaks characterized by mostly strike-slip faulting.

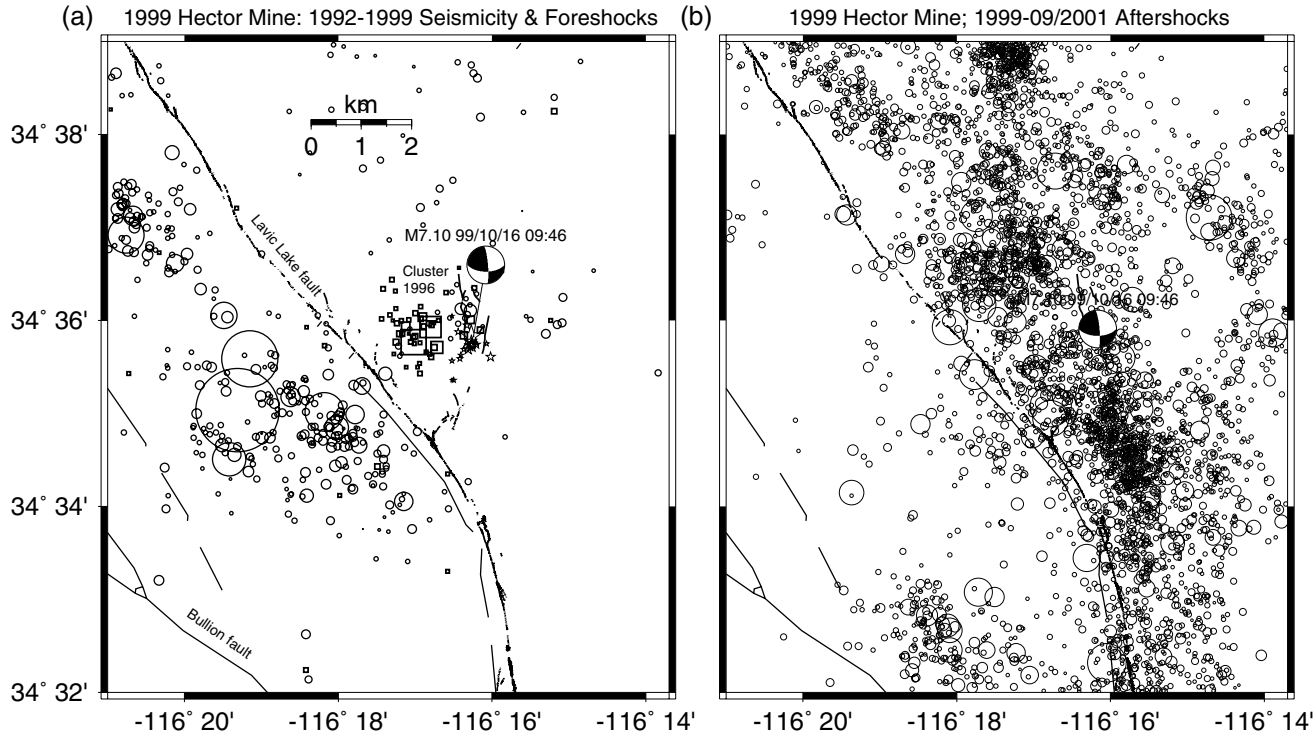

Figure 4. (a) The background seismicity in the Hector Mine epicentral area from 1981 to October 1999; relocations using 3D velocity models (Hauksson, 2000). The map area covers the square symbol for the mainshock in Fig. 1. The seismicity that followed the 1992 Landers mainshock is shown as circles and the 1996 cluster is shown as squares. The foreshocks to the Hector Mine mainshock are shown as stars. (b) The Hector Mine aftershocks in the same region from 16 October 1999 to September 2001. The aftershocks are mostly located to the east of the two previous sequences in the area.

These surface breaks had the same strike as the N6°W nodal plane of the first-motion focal mechanism.

The first-motion focal mechanism of the mainshock, which describes the very first rupture initiation, has one nodal plane striking N6°W and dipping 85° to the east, which also coincides with the orientation of the main surface break to the south. The dip of this nodal plane may be vertical, because it is constrained only to $\pm 10°$. This mechanism differs from the mechanism determined from the regional SCSN/TriNet waveform data, which showed the mainshock nodal plane striking N29°W with a dip of 77° to the east (Scientists of the USGS, *et al.*, 2000). This difference could be attributed to the waveform focal mechanism being dominated by the waves radiated from the N30°W-striking segment, located 5 km to the south of the mainshock epicenter.

Aftershocks

The aftershocks are distributed across a wide region, with at least four distinct zones. In Figure 6 we show relocations of aftershock determined by applying both 3D Vp and Vp/Vs models (Hauksson, 2000) and double-difference methods (Waldhauser and Ellsworth, 2000). A N6°W-striking zone extends north and south of the mainshock epicenter. A N30°W-striking zone parallels the Bullion fault surface rupture to the south. Another N30°W-striking zone extends east of the Lavic Lake fault, verging into the N6°W zone north of the mainshock. The fourth zone is a diffuse cluster of events, spatially separate from the rest of the aftershocks and located 10 km north of the north end of the mainshock rupture. This broad distribution of aftershocks suggests a volumetric strain release modulated by the tectonic fabric and the regional tectonic stress. The mainshock epicenter is located near the middle of this distribution, at the northern end of the N6°W segment.

N6°W-striking trends of aftershocks extend both north and south of the mainshock, but are offset from each other at the mainshock epicenter. The northern trend is offset about 2 to 3 km to the west with respect to the southern trend. The continuous southern trend ends at the Bullion fault, but picks up again for a short section 5 km south of the Bullion fault where two of the largest aftershocks (*M* 5.7 and *M* 5.0) occurred. All three of the N6°W-striking sections appear to have a vertical dip (Fig. 7). In contrast, the N30°W-striking clusters dip to the northeast (cross sections B and E, Fig. 7). The southern N30°W cluster corresponds to the mainshock rupture on the Bullion fault and is planar enough to be assigned to that fault. This cluster also extends northwest of the intersection with the N6°W trend. The N30°W-

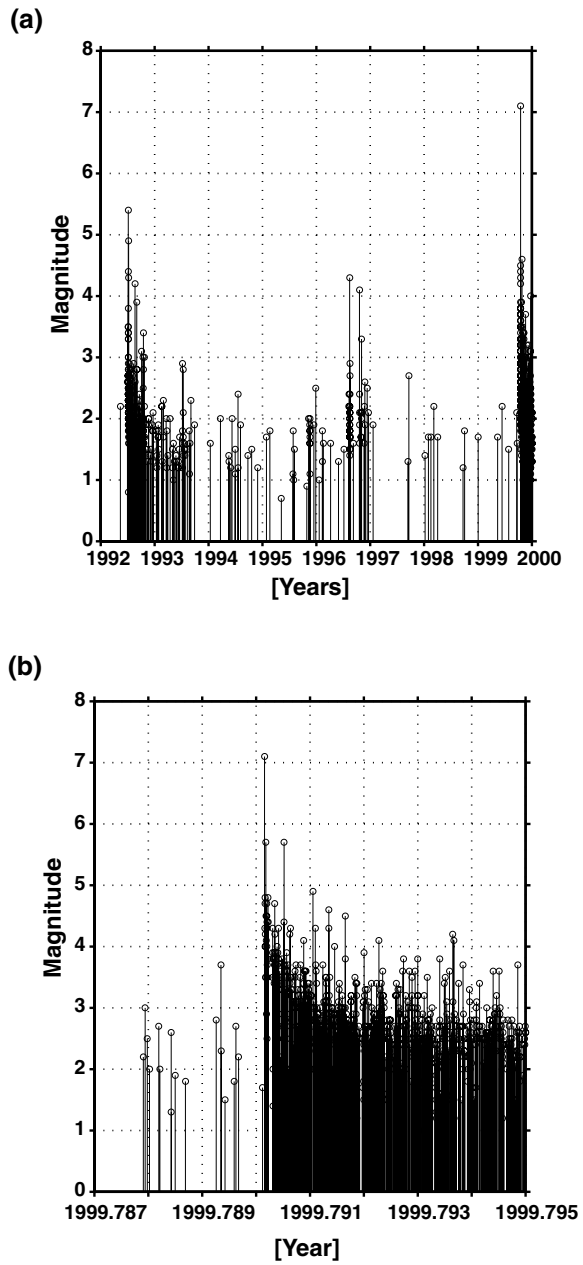

Figure 5. (a) Magnitude versus time plot for the background seismicity shown in Fig. 4a. (b) Magnitude versus time plot showing the Hector Mine foreshocks and aftershocks. This figure was made using ZMAP (Wiemer, 2000).

striking cluster at Lavic Lake is more diffuse than the southern cluster, suggesting a more volumetric deformation of the block of crust between the two northern strands of the mainshock rupture surface.

Like the Landers earthquake, the Hector Mine earthquake triggered aftershocks offset to the north of the mainshock rupture. The three Hector Mine clusters, north of Interstate 40 and Lavic Lake, are about 10 km north (25% of the mainshock fault length) of the other aftershocks. (Fig. 6). The Barstow cluster associated with the Landers earthquake was located about 40 km (50% of the mainshock fault length) north of the other Landers aftershocks (Fig. 1). Three major Hector Mine clusters, north of Interstate 40, had several late, large $M > 4$ aftershocks (Fig. 6).

The two mainshock asperities, with highest slip from Ji *et al.* (2002), do not obviously contribute significantly to the distribution of the aftershocks. The mainshock first-motion nodal plane strike of N6°W, where about 41% of the seismic moment was released (Ji *et al.*, 2002), has a broad distribution of aftershocks associated with it. Further, along the N30°W-striking Lavic Lake fault, the area of second-highest moment release (Ji *et al.*, 2002), there are almost no aftershocks in the immediate vicinity of the rupture plane.

The depth distribution of aftershocks varies along the rupture zone from north to south. The aftershocks located to the north of Interstate 40, which have better depth constraints, are shallower, extending to depths of 8 to 10 km (Fig. 7). Along the central part of the rupture, the aftershocks extend to depths of 10 to 12 km. About 30 km south of the mainshock epicenter, they extend only to depths of 6 to 8 km.

The apparent dip of fault segments, and possibly both horizontal and vertical en echelon offsets of fault segments, contribute to the complex distribution of aftershocks. The depth sections of aftershocks in Vp cross sections that are taken orthogonal to the trend of aftershocks show mostly steeply dipping aftershock distributions, which in some cases can be interpreted to have en echelon offsets in depth (Fig. 7). The N6°W-striking faults are vertical, while the N30° to 40°W-striking segment of the Lavic Lake fault dips 80° to 90° to the east (Figs. 7B and C). Similarly, to the south, in cross sections D and E, the N30°W Bullion fault appears to have a dip of 70° to 80° to the east. An alternative interpretation, supported by dips of nodal planes of aftershock focal mechanisms, as discussed later, is that all of these fault segments are vertical and an apparent dip is created by en echelon offsets in depth.

3D Vp and Vp/Vs Models

The Vp velocity structure in the region of the Hector Mine earthquake sequence is similar to the average structure for the Mojave region (Hauksson, 2000). The near-surface Vp ranges from 4.5 to 5.5 km/sec down to depths of 5 km and gradually increases to 6.2 km/sec at 10 to 14 km depth. Some minor low velocity basins can be seen within the northern near-surface part of the model. At depth, the Vp model shows a smoothly varying Vp structure, with only a few short wavelength anomalies of high or low Vp. The foreshocks and mainshock occurred adjacent to one of these anomalies of Vp contrast, with higher Vp on the east side than on the west side (Fig. 7).

In some cases these Vp anomalies also appear to influence the distribution of aftershocks, although there is not a simple relationship between the depth distribution of aftershocks and the Vp model. To the north, where there are

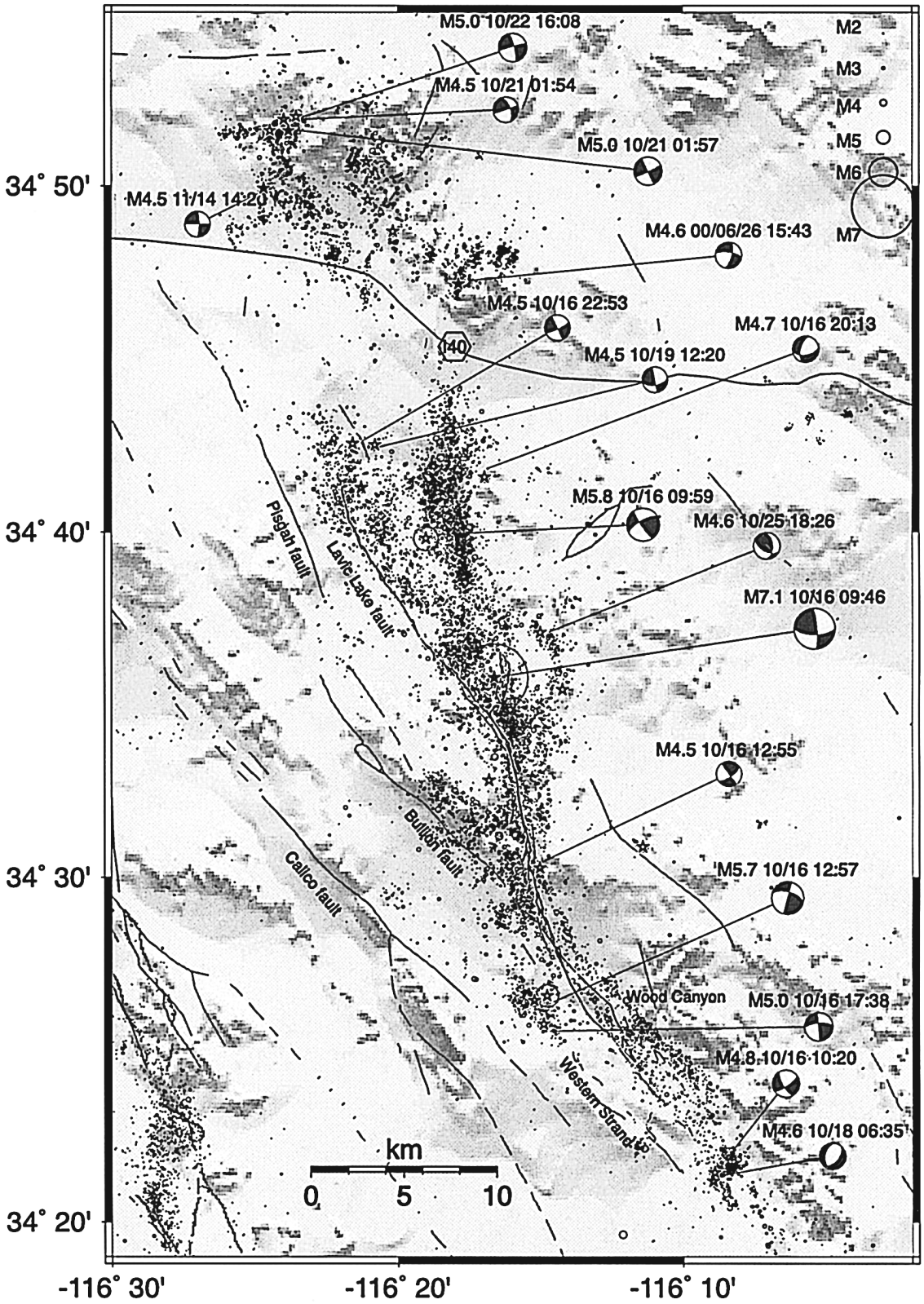

Figure 6. Map view of the Hector Mine mainshock and aftershocks. Mapped surface rupture from Treiman *et al.* (2002). The $M \geq 4.5$ earthquakes are plotted as stars and their first-motion focal mechanisms are also shown, labeled with the magnitude, date, and time. The symbol size is scaled with magnitude, as is shown by the scale to the upper right. These aftershock hypocenters were refined using the double-difference algorithm of Waldhauser and Ellsworth (2000).

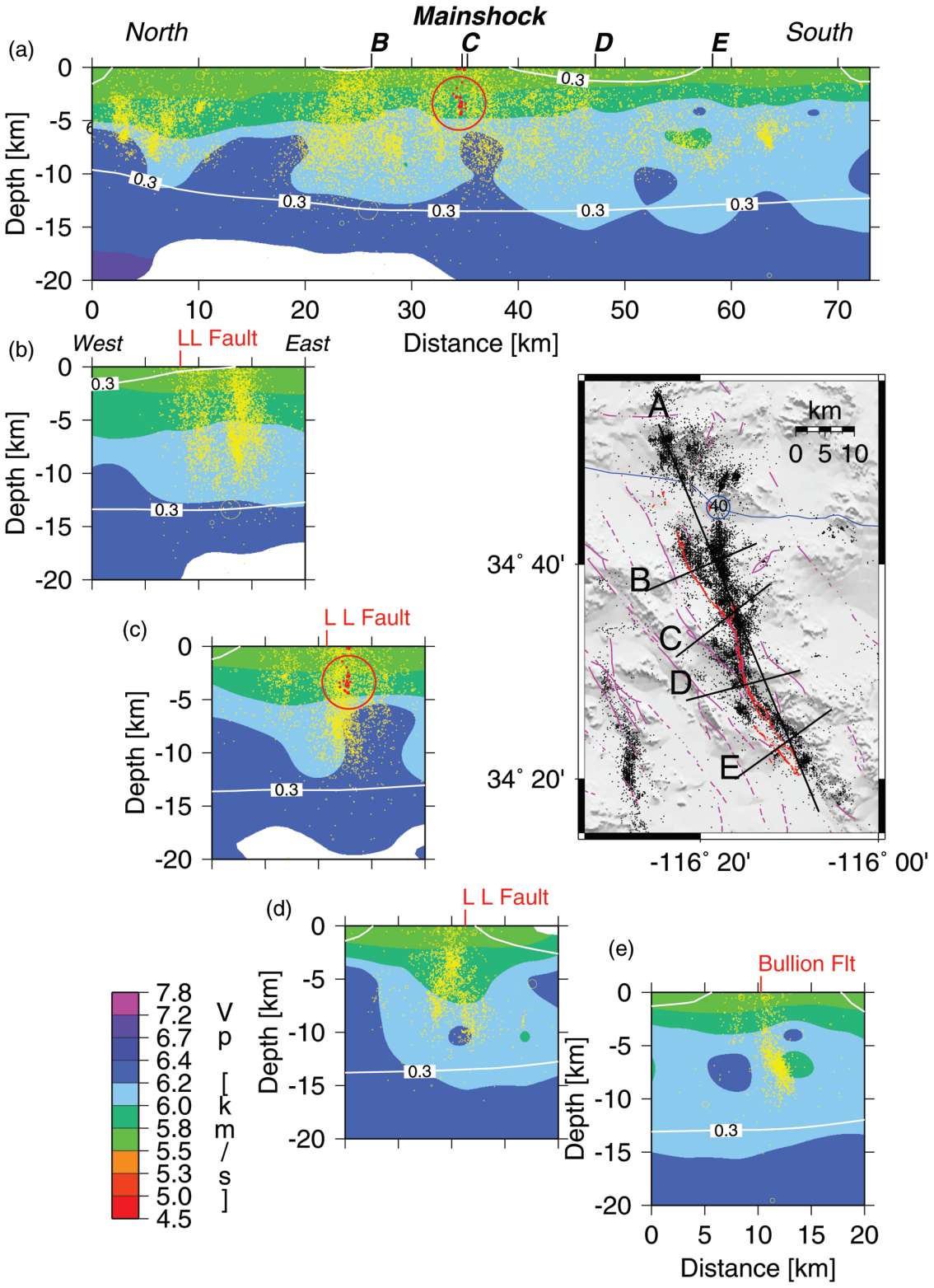

Figure 7. Cross sections showing Vp 3D model and Hector Mine aftershocks within 5 km distance; the map shows the location of the cross sections. The model is well resolved within the 0.3 contour line of the diagonal elements of the resolution matrix. Only model areas with adequate ray coverage are shown in color. (a) Vp cross section along the strike of the fault, foreshocks and mainshock shown in red; (b) Vp cross section to the north of the mainshock epicenter; (c) cross section across the foreshock and mainshock hypocenters shown in red; (d) cross section across the intersection of the Lavic Lake (LL) and Bullion faults; (e) cross section across the Bullion fault.

fewer aftershocks, the 6.2 km/sec contour extends to a shallower depth (Fig. 7a). The aftershock density decreases significantly as the Vp increases from 6.2 to 6.4 km/sec, which probably coincides with the bottom of the mainshock rupture (Ji *et al.*, 2002). At depths greater than 15 km, where there are fewer aftershocks, the model is not well resolved, as indicated by the 0.3 contour of the diagonal element of the resolution matrix.

The Vp/Vs model is similar to the average Vp/Vs structure in the Mojave Desert region, as well as elsewhere in southern California (Hauksson, 2000). The final model has Vp/Vs in the range of 1.62 to 1.82, reflecting the subtle variations in the crustal structure (Fig. 8). In general, the geometrical shapes of the Vp/Vs anomalies are different from the shapes of the Vp anomalies, with at least three low Vp/Vs anomalies along the strike of the mainshock rupture, in the depth range of 5 to 12 km. Because these anomalies are mostly of low Vp, they may be indicative of quartz-rich granitic intrusions (McCaffree Pellerin and Christensen, 1998). The Vp/Vs anomalies from 10 to 15 km depth are tabular in shape and suggest alternating layers of high and low Vp/Vs. These layers may be related to rock composition or less likely to fluid-filled cracks. Possible small changes in rock composition with depth that may include intrusive mafic rocks in the lower crust are sufficient to explain these anomalies. Mapped Miocene and Holocene volcanic rocks in the region are evidence for the presence of intrusive mafic rocks (Dibblee, 1967; Bortugno and Spittler, 1986)

The aftershock distribution appears to be more strongly related to the Vp/Vs model than to the Vp model. The aftershocks mostly occur within regions of moderate Vp/Vs values, but are absent within regions of very low or high Vp/Vs. The cross sections, taken orthogonal to the rupture, show lateral variations in the Vp/Vs model. In particular, near the hypocenter of the mainshock, the high Vp/Vs occurs to the west but the high Vp occurred to the east. Similarly, the zone of dipping aftershocks beneath the Bullion fault coincides with a region of intermediate Vp/Vs, with a region of high Vp/Vs to the west (Fig. 8C). The high Vp/Vs on the west side of the mainshock rupture may be related to the presence of a Jurassic diorite body to the west (Langenheim and Jachens, 2002). Thus, most of the Vp/Vs spatial variations may be related to changes in composition, and the mainshock rupture may mostly control the distribution of aftershocks.

The role of fluids in the physics of earthquakes in southern California is poorly understood. Small changes in rock composition in the region of the Hector Mine earthquake are sufficient to explain the Vp and Vp/Vs anomalies; the presence of fluids is not required. In a different study, Zhao *et al.* (1996) determined tomographic Vp and Vp/Vs models and, based on a high (up to 6%) Poisson's ratio anomaly, suggested the presence of fluids at the hypocenter of the 1995 M_w 7.2 Kobe earthquake in Japan. In a study of seismicity beneath the eastern North Island of New Zealand, Reyners *et al.* (1999) suggested that background seismicity and in some cases aftershocks occurred in volumes of intermediate Vp/Vs, surrounding the mainshock rupture zone of high Vp/Vs. Although a similar pattern may exist for the Hector Mine earthquake, it cannot easily be resolved with existing data.

Aftershock Statistics

The aftershocks of the Hector Mine sequence have followed a normal pattern of decay. The rate of aftershocks can be described by

$$\lambda = 10^{[a - b(M - M_m)]} \cdot (t + c)^{-p},$$

where M is the magnitude of the aftershock, M_m is the magnitude of the mainshock, t is time since the mainshock, and a (a-value), b (b-value), p (p-value), and c (c-value) are parameters (Reasenberg and Jones, 1989). The rate of decay for the Hector Mine sequence was slightly above the mean for southern California, with a p-value of 1.11 ± 0.06. The b-value was also above the mean, at $b = 1.04 \pm 0.07$.

The three large aftershock sequences in the Mojave Desert in the 1990s have similar bulk aftershock parameters. Although there are significant local spatial variations in the b- and p-values along strike of the fault planes (Wiemer *et al.*, 2002), these parameters averaged over the whole sequences for Joshua Tree (M 6.1, 1992), Landers (M 7.3 1992), and Hector Mine are quite similar (Table 1). This might suggest that the bulk p- and b-values result from the shared local tectonics of these sequences. In contrast, the a-value, a measure of the overall productivity of the aftershock sequences, varies significantly, with Joshua Tree having the highest and Hector Mine the lowest values. This could be interpreted as a decrease with time, or a decrease with lower strain rate as the distance from the San Andreas fault increases.

Focal Mechanisms of Aftershocks

The focal mechanisms of the aftershocks are diverse, although strike-slip and normal-faulting focal mechanisms are most common. Of the 21 large aftershocks of $M_L \geq 4.5$ that have first-motion focal mechanisms available, 19 exhibit mostly strike-slip faulting. The strike of these aftershocks corresponds with its location in a N6°W or N30°W trend (Table 2). Many of the $M_L \geq 4.5$ aftershocks occurred in pairs within dense clusters of aftershocks that are located towards the end of rupture segments or in regions of bends in the fault rupture (Fig. 6).

Similar to the first-motion focal mechanism of the mainshock, the hypocenters of the second largest aftershock of M_L 5.7 and a M_L 5.0 aftershock define a N6°W trend, 18 km south of the mainshock (Fig. 6). Both of these aftershocks occurred about 2 km south of the mapped surface rupture in the offset N6°W cluster. This trend also coincides in strike with the M_L 4.7 and M_L 4.6 aftershocks, 11 and 21 km to the north of the mainshock, respectively. Thus, the influence

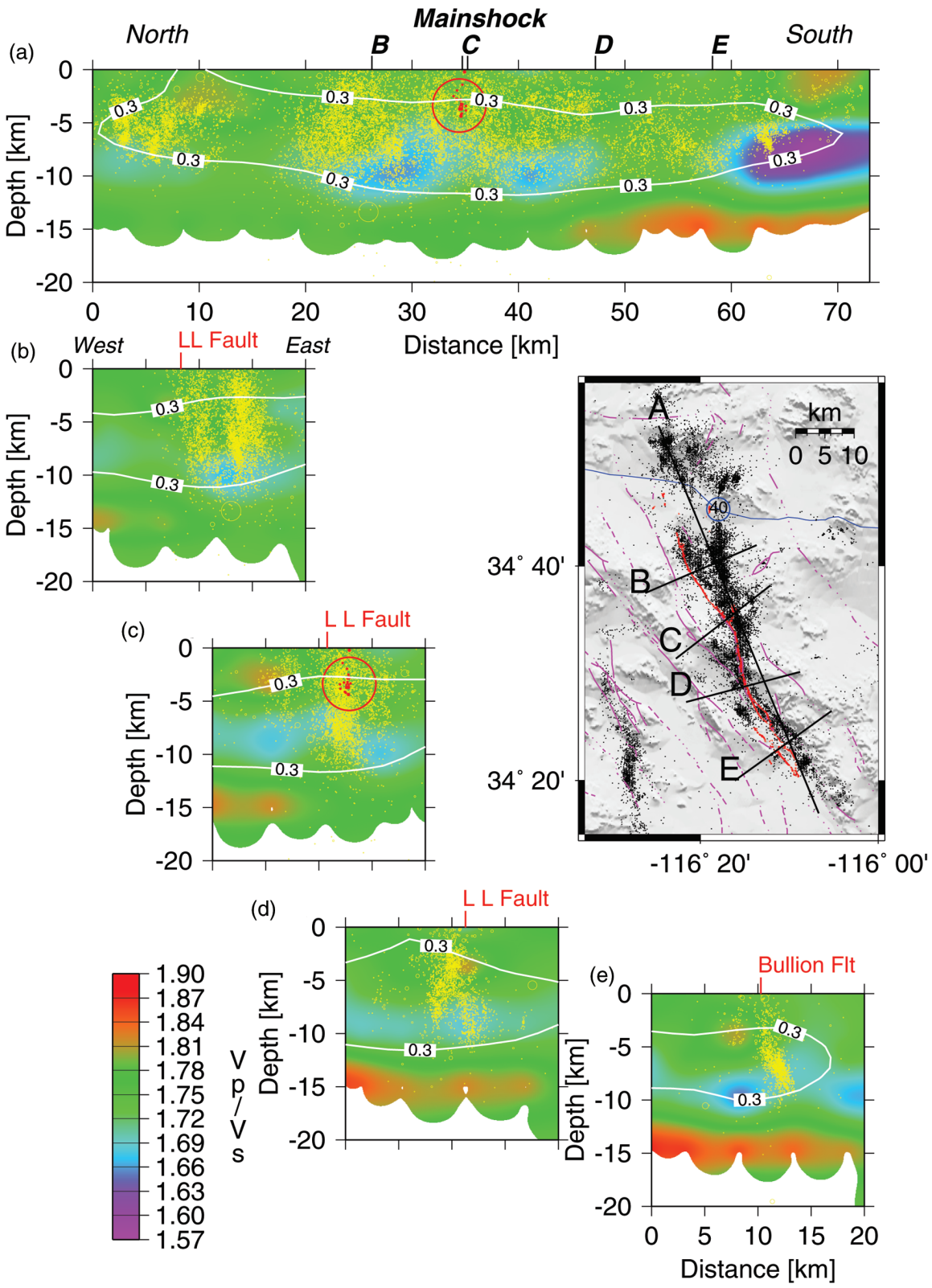

Figure 8. Cross sections showing Vp/Vs 3D model and Hector Mine aftershocks within 5 km distance, the map shows the location of the cross sections. The model is well resolved within the 0.3 contour line of the diagonal elements of the resolution matrix. Only model areas with adequate ray coverage are shown in color. For details see the caption of Fig. 7.

Table 1
Parameters Describing Earthquake Sequences in the ECSZ

Earthquake Sequences	*b*-value	*p*-value (decay)	*a*-value (productivity)	*c*-value
Joshua Tree	1.07 ± 0.05	1.14 ± 0.05	−1.70 ± 0.17	0.18
Landers	1.03 ± 0.03	1.14 ± 0.02	−1.97 ± 0.14	0.43
Hector Mine	1.04 ± 0.07	1.11 ± 0.06	−2.45 ± 0.29	0.21
Average for Southern California	0.92	1.05	−1.85	0.05

of the N6°W strike of the mainshock faulting extends over a distance of almost 40 km. In contrast, the largest aftershock of M_L 5.8 that occurred within 13 minutes of the mainshock and was located 9 km to the north-northwest at a depth of 14 km, had a strike of N30°W (Fig. 6). The dip of the N30°W-striking nodal plane is 90°, suggesting that this aftershock occurred on a subparallel fault to the Lavic Lake fault that ruptured in the mainshock. This observation of nodal plane dip is important because it contradicts the interpretation that the aftershocks along the Lavic Lake fault dip to the east.

Toward the south end of the N30°W segment of the Bullion fault, a cluster of aftershocks occurred, including M_L 4.8 and M_L 4.6 at the end of the mapped surface rupture. These both had a strike of N35°W. The two dip-slip $M \geq 4.5$ events are located in the region to the north and northeast of the mainshock, near the edge of the densest part of the aftershock distribution (Fig. 6). One exhibits north-northwest-striking thrust faulting and the other north-northeast-striking normal faulting. To the west of these events, the N35°W-striking north branch of the Lavic Lake fault has no large aftershocks for a distance of 15 km. The focal mechanisms in the cluster of aftershocks north of the surface rupture and Interstate 40 are more diverse, with a mixture of strike-slip and normal faulting. The strike of the right-lateral plane in the strike-slip mechanisms is much more variable than in the region surrounding the mainshock rupture surfaces.

The first motion focal mechanisms for more than 1400 aftershocks show a distribution as complex or more than the $M \geq 4.5$ events already discussed. A sample of focal mechanisms from the south-central rupture segment is shown in Figure 9. Along the N6°W trend defined by the mainshock nodal plane, there are several events with similar strike-slip solutions. In their immediate vicinity both normal and thrust faulting mechanisms occur. These dip-slip mechanisms have either northeast-, north-, or northwest-striking nodal planes. This diversity continues to the south along the Lavic Lake fault as it merges with the Bullion fault. The focal mechanisms along the northwest segment of the Bullion fault are predominantly normal faulting, consistent with counterclockwise rotation of the adjacent Bullion Mountains western block (Fig. 9).

State of Stress

We invert focal mechanisms from both the preseismicity and the aftershocks for the state of stress, to identify both temporal and spatial variations in the regional stress field (Table 3). In all cases, the stress state is well constrained, with 95% confidence limits of approximately ±10°. Most of the stress changes consist of variations in the trend of the two horizontal principal stresses, the maximum principal stress, S_1, and the minimum principal stress, S_3, and small variations in the value of ϕ, the stress ratio (Michael, 1984). In all cases, the intermediate principal stress, S_2, remains near vertical, consistent with strike-slip faulting.

The limited spatial extent of the background seismicity makes it difficult to compare the state of stress before and after the mainshock. We chose the area shown in Figure 4, where there was some previous seismicity, and inverted the focal mechanisms of background seismicity near the mainshock epicenter and the aftershocks (Fig. 10). To search for possible variations in the state of stress, we divide the rupture zone into four segments, from north to south, and determine the state of stress from the focal mechanisms of the aftershocks. For each region, we invert for the orientation of the three maximum principal stresses and their relative sizes (Figs. 11 and 12).

In general, the state of stress is strike-slip with a vertical intermediate principal stress. In the aftershocks, the maximum horizontal stress trends N42° to 54°E in the three regions to the north (A–C) and varies significantly only in the south region (D), near the Bullion fault, where it rotates counterclockwise to N25°E (Fig. 12). The trend of the maximum horizontal stress for the background seismicity is N28°E. This agrees with the results of Unruh *et al.* (1996), who used the 1992 to 1994 earthquakes to determine the azimuth of the minimum principal strain-rate axis as shortening in the direction N34°E. This suggests a rotation of the state of stress at the mainshock epicenter of 10° to 15° to the east during the mainshock; however, this result is not significant within the 95% confidence limits. The angle between the maximum horizontal stress and the rupture plane at the epicenter is 34°, thus suggesting a normal frictional value for the N6°W-striking fault segment.

The 17° to 29° more northerly stress direction along the south end of the rupture probably existed prior to the mainshock. If a rotation of the stress field had occurred, it would have been a rotation to the east and thus would have decreased the difference between north and south. The initial stress field forms an angle of 65° with the Bullion fault and thus could have contributed to the termination of the mainshock rupture. This high angle between the stress direction and the fault strike is similar to the stress direction and the strike of the Camp Rock fault at the northern end of the 1992 Landers earthquake rupture (Hauksson, 1994).

The results of the stress inversions for the Hector Mine data are consistent with the ECSZ forming one of several stress refractors in southern California (Hauksson, 1994).

Table 2
Hypocenters of Hector Mine Foreshocks, Mainshock, and M > =4.5 Aftershocks

Date	Time (UTC)	Latitude	Longitude	Depth (km)	Mag	#PH	rms (sec)	ERH (km)	ERZ (km)	DDR	Dip	Rake	#FM	CUSP-ID
Foreshocks														
1999	10 15 14 22 43.6	34N35.82	−116W16.15	03.0	3.05	51	0.10	1.3	0.8	355	85	−10	35	9108537
1999	10 15 16 35 54.3	34N35.74	−116W16.11	03.0	2.72	29	0.07	1.5	2.2	165	90	10	19	9108545
1999	10 16 01 55 38.9	34N35.83	−116W16.14	02.6	2.89	43	0.06	0.1	6.4	95	55	170	25	9108593
1999	10 16 02 41 04.7	34N36.03	−116W16.10	01.9	3.73	67	0.20	1.8	4.6	85	90	−160	58	9108606
1999	10 16 05 07 10.0	34N35.85	−116W16.19	03.2	2.76	47	0.08	0.1	7.8	190	65	−10	27	9108633
1999	10 16 05 33 48.3	34N35.94	−116W16.28	02.3	2.27	31	0.06	0.1	8.6	75	90	160	12	9108627
Mainshock and Aftershocks														
1999	10 16 9 46 44.1	34N35.98	−116W16.08	02.0	7.10	53	0.10	1.4	2.2	180	65	10	42	9108652
1999	10 16 9 51 48.4	34N26.44	−116W15.38	03.4	4.87	48	0.10	0.2	0.9					3320846
1999	10 16 9 52 53.4	34N31.19	−116W 9.95	06.8	4.74	22	0.14	0.7	2.4					3320847
1999	10 16 9 59 35.2	34N40.34	−116W18.31	13.1	5.79	41	0.12	0.4	8.1	330	70	10	29	3320848
1999	10 16 10 2 39.8	34N34.88	−116W16.06	01.1	4.52	42	0.09	0.4	1.2					3320849
1999	10 16 10 7 29.9	34N48.01	−116W16.73	03.6	4.76	49	0.18	0.2	1.9					9108646
1999	10 16 10 8 4.4	34N42.49	−116W20.42	08.5	4.58	32	0.10	0.2	1.3					9108676
1999	10 16 10 20 52.8	34N21.80	−116W 8.75	02.6	4.83	55	0.17	2.7	5.8	145	75	−20	33	9108709
1999	10 16 11 26 4.5	34N48.70	−116W20.55	−0.5	4.70	32	0.11	0.2	1.6					9108775
1999	10 16 12 55 9.8	34N30.40	−116W15.47	03.2	4.47	41	0.14	2.3	2.5	145	90	20	23	9108881
1999	10 16 12 57 21.2	34N26.45	−116W14.77	06.2	5.70	52	0.08	0.2	7.4	105	90	−150	45	3320736
1999	10 16 17 38 48.8	34N25.79	−116W14.64	04.7	4.95	81	0.15	1.9	1.7	85	90	−160	51	9109254
1999	10 16 20 13 37.5	34N41.85	−116W16.84	02.4	4.68	63	0.13	1.5	1.7	170	55	−40	56	9109442
1999	10 16 22 53 41.1	34N42.65	−116W21.46	07.4	4.52	68	0.13	0.2	5.5	65	90	170	71	9109636
1999	10 18 6 35 47.2	34N21.58	−116W 8.61	00.5	4.64	69	0.17	2.0	6.6	130	50	−70	67	9111353
1999	10 19 12 20 44.2	34N42.56	−116W20.61	08.0	4.52	46	0.09	0.2	5.2	170	55	0	51	9112735
1999	10 21 1 54 6.5	34N52.04	−116W24.01	03.7	4.47	47	0.09	0.1	2.8	160	90	30	40	3320883
1999	10 21 1 54 33.9	34N52.58	−116W23.92	01.2	5.06	53	0.11	0.2	0.3					3321590
1999	10 21 1 57 38.6	34N51.74	−116W23.86	03.4	4.97	72	0.09	0.1	21.1	155	85	0	87	3320884
1999	10 22 16 8 48.0	34N51.76	−116W24.24	02.6	5.04	70	0.11	0.1	27.1	345	85	−10	117	9114812
1999	10 25 18 26 0.6	34N37.09	−116W14.39	02.3	4.64	43	0.07	1.1	0.8	210	55	50	48	3321011
1999	11 14 14 20 9.3	34N49.97	−116W24.53	06.3	4.49	56	0.10	0.1	3.0	90	80	−180	62	9122706
2000	06 26 15 43 7.4	34N47.15	−116W17.68	04.8	4.56	73	0.10	0.1	2.1	105	70	−160	61	9155518

Mag, local magnitude; #PH, number of phases used in the solution; rms, root mean square residual; ERH, horizontal error; ERZ, vertical error; DDR, dip direction of the nodal plane; #FM, number of first motions; CUSP-ID, database identification number.

The 1992 Landers earthquake sequence showed similar maximum principal stress orientations as those of the Hector Mine sequence. The maximum stress direction in both sequences is rotated to the east from the northerly regional maximum stress direction. This rotation in stress directions is similar to the rotation determined from the 1981-to-1998 background seismicity by Hardebeck and Hauksson (2001). Both geological and geodetic data show that ECSZ concentrates shear strain. This concentration of strain, together with the stress rotations in the background seismicity, Hector Mine, and Landers sequences, suggests that the ECSZ, like the San Andreas fault, is a weaker zone that modifies the regional stress field.

Discussion

The ECSZ has accommodated approximately 65 km of right shear over the last 2 to 3 Ma or 22% to 25% of the total motion along the Pacific–North America plate boundary (Dokka and Travis, 1990b). The right-lateral shear takes place over an 80-km-broad zone of deformation, and includes the complex behavior of many major strike-slip faults and numerous dip-slip faults. Major earthquakes such as the 1992 M_w 7.3 Landers and the 1999 M_w 7.1 Hector Mine events vividly illustrate this crustal deformation.

Complex Conjugate Faulting

The Hector Mine mainshock ruptured along several fault segments with different orientations and was followed by an even more complex aftershock sequence. One possible interpretation of this distributed strike-slip faulting is that it was volumetric and was accommodated through slip on many different conjugate planes. First, the mainshock broke a N6°W fault segment for a distance of 15 km. Second, it ruptured along two segments, forming a 30° angle to the first trace (Ji *et al.*, 2002; Treiman *et al.*, 2002). In addition, the focal mechanisms of the aftershocks exhibit a complex mixture of strike-slip and dip-slip faulting; however, the orientation of the maximum principal stress is not such that both planes are favorably oriented for faulting.

The regional tectonic stress varies across the region. The maximum horizontal stress forms a 30° to 35° angle to the

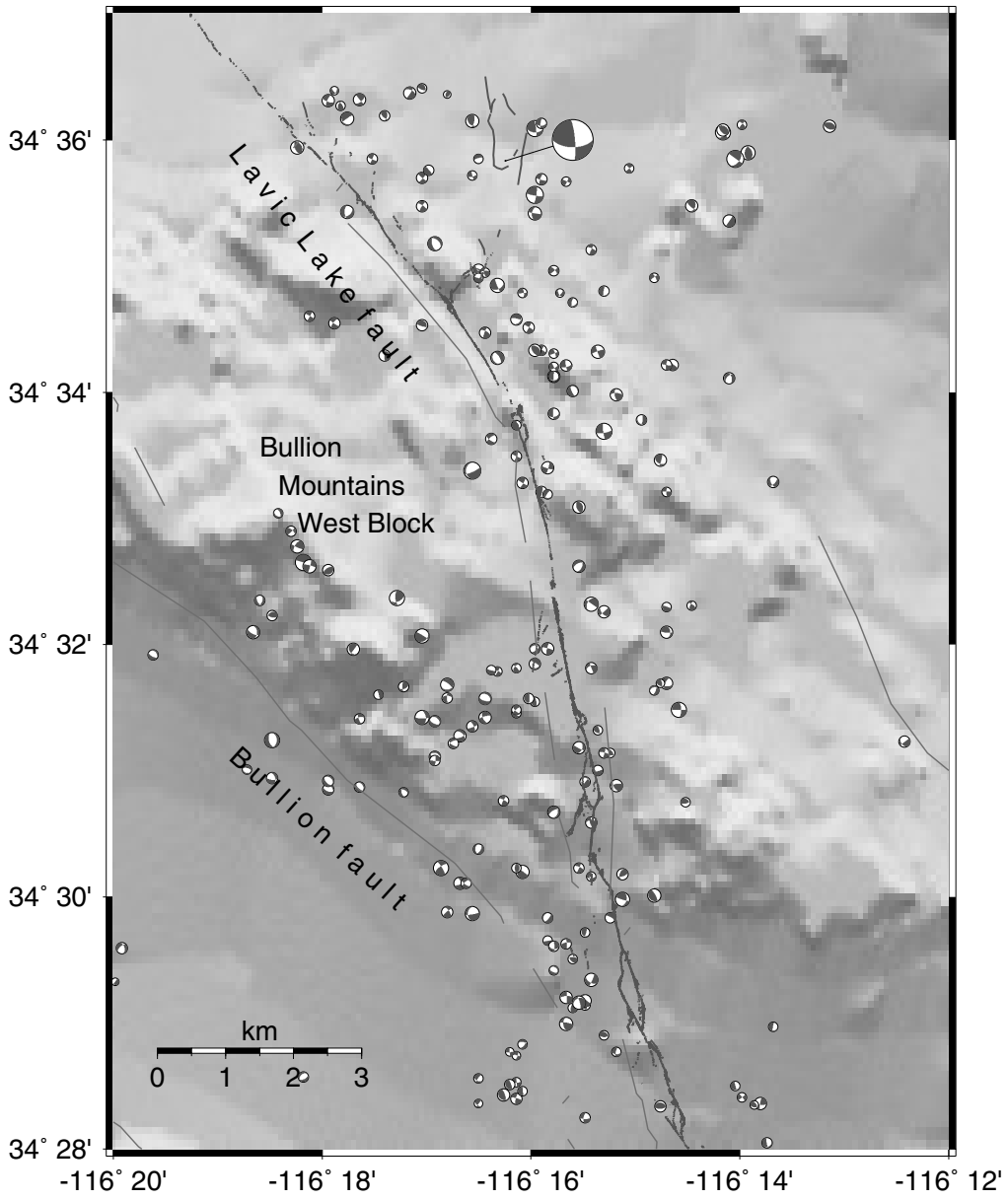

Figure 9. Lower-hemisphere, first-motion focal mechanism of $M \geq 2.0$ aftershocks with 12 or more first motions; south-central region (region C) located to the south of the mainshock epicenter (see also Fig. 12). Compressional quadrants are shaded.

Table 3
Stress Inversion Results for the Hector Mine Sequence

Region	Number of Planes	ϕ	Maximum Principal Stress		Intermediate Principal Stress		Minimum Principal Stress		Average Misfit Angle (β)	
			Trend	Plunge	Trend	Plunge	Trend	Plunge	Mean	S.D.*
Preseismicity (Fig. 4a)	46	0.34	−152°	10°	83°	73°	−60°	13°	37°	32°
Aftershocks (Fig. 4b)	187	0.44	48°	09°	−65°	67°	142°	21°	48°	45°
(A) North Region	369	0.64	−138°	04°	39°	86°	131°	00°	36°	25°
(B) North Central Region	313	0.60	43°	09°	−157°	80°	−47°	03°	47°	39°
(C) South Central Region	205	0.63	54°	31°	−100°	56°	152°	12°	66°	49°
(D) South Region	212	0.56	25°	11°	−153°	79°	115°	00°	47°	41°

*Standard deviation.

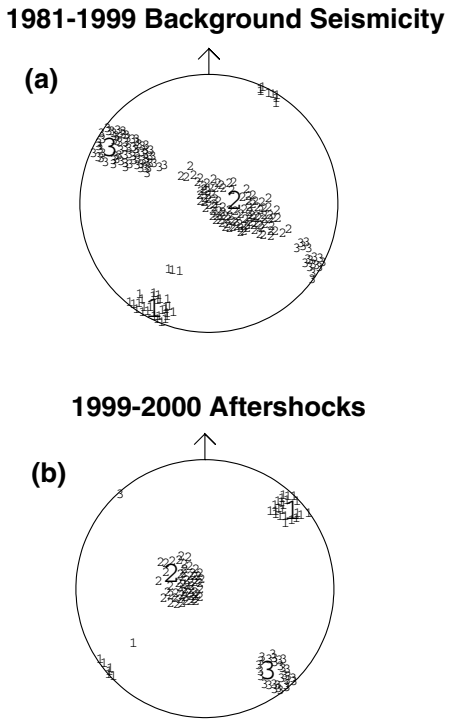

Figure 10. (a) The stress state showing the orientation of the three principal stresses (designated by large 1, 2, and 3) and their 95% confidence limits (designated by small 1, 2, and 3), determined from focal mechanisms of the background seismicity (1981 to October 1999) shown in Fig. 4a. (b) The corresponding stress state for the aftershocks in the same area as shown in Fig. 4b.

N6°W faults where the rupture initiated and thus was conducive to failure in classical mechanics. The N35°W faults in the north form a 60° to 65° angle, while the N35°W faults in the south form a 45° to 50° angle to the maximum horizontal stress. Both of the N35°W faults are at a high angle to the maximum stress and would require significantly lower friction or an alternative dynamic process to sustain failure. Because the rupture started on the N6°W segment, it is possible that the combination of regional stress, fault strike, and coefficient of friction results in faults of similar effective strength. The complexity in aftershock focal mechanisms also suggests a similar stress field heterogeneity or dynamic fluctuations.

Relation to the 1992 Landers Earthquake

One of the many puzzling observations about the occurrence of the Hector Mine earthquake is its location, about 20 km to the east of the 1992 M_w 7.3 Landers rupture. Because the tectonic strain rate decreases from west to east, away from the San Andreas fault, a more likely location might have been to the west of Landers, where the high San Andreas strain rates start to play a role. Alternatively, the next major earthquake in the ECSZ should have occurred to

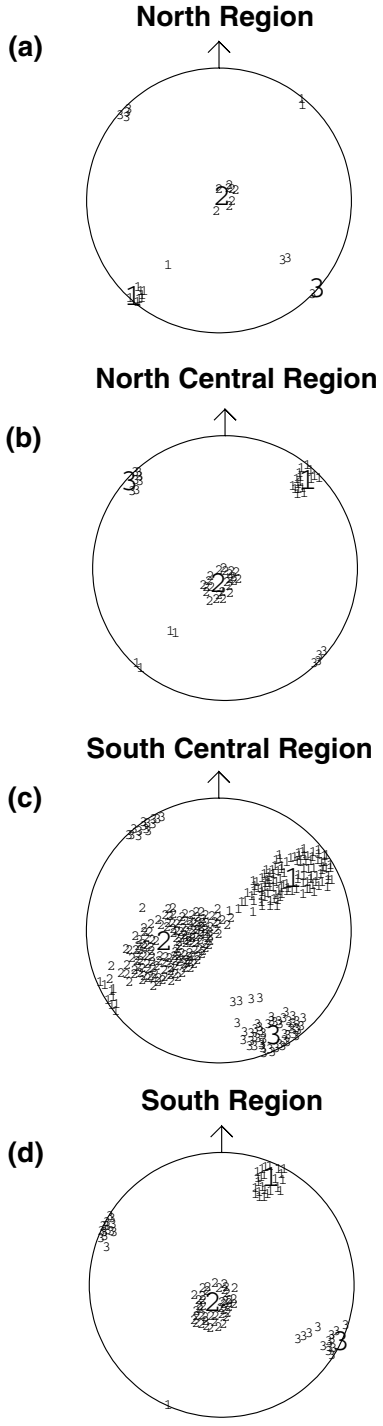

Figure 11. Stress states determined from first-motion focal mechanisms of aftershocks divided into: (b) north region, A; (c) north-central region, B; (d) south-central region, C; and (e) south region, D. The orientation of the three maximum principal stresses and their 95% confidence limits are shown; see also Table 3.

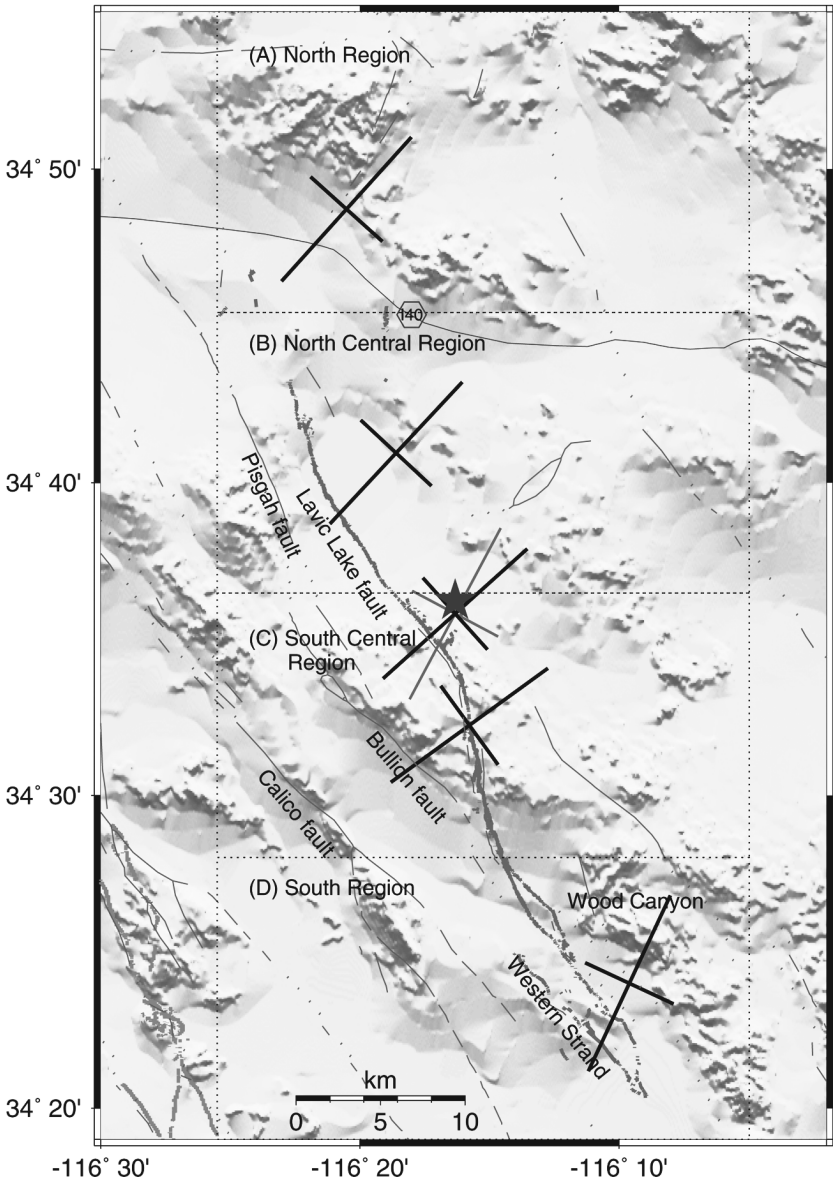

Figure 12. Stress directions (crosses) determined from the focal mechanisms that are located within each of the four regions outlined by dashed lines. The longer axis is the maximum horizontal stress and the shorter axis is the minimum horizontal stress. The background stress is shown as thin lines and the epicenter of the M_w 7.1 mainshock as a star.

the north, extending the strain release toward the Garlock fault and into the southwestern Basin and Range province.

The seismological similarities of the 1992 M_w 7.3 Landers and the 1999 M_w 7.1 Hector Mine earthquakes include similar foreshock sequences (Hauksson *et al.*, 1993), similar initial strike of the rupture (N6° to 10°W), and rupture along many fault strands. The seismological differences between the two sequences include opposite rupture directions, more spatially distributed aftershocks for Hector Mine, and somewhat shallower faulting for the Hector Mine mainshock and aftershocks.

Both the 1992 Landers and 1999 Hector Mine earthquakes occurred on multiple strike slip faults. Sieh *et al.* (1993) showed that the slip in the 1992 M_w 7.3 Landers earthquake extended for 85 km and was on the average 2 to 4 m, with maximum slip of 6 m. The Camp Rock fault had a slip of mostly less than 1 m. Treiman *et al.* (2002) show that the rupture length of Hector Mine rupture was 40 km and the average slip 1.5 m, with a maximum of 5.3 m. When the Landers rupture reached the Camp Rock fault, it appeared to involve mostly shallow faulting and was not associated with significant aftershock activity. The 1999 Hector Mine mainshock broke to the south-southeast along the Bullion fault and showed a similar behavior. The aftershocks become significantly shallower to the south, and the amount of slip decreases rapidly (Ji *et al.*, 2002; Treiman *et al.*, 2002).

The spatial distribution of the surface rupture and aftershocks of the 1992 Landers and 1999 Hector Mine earthquakes may be related to a crustal heterogeneity or to existing faults. Langenheim and Jachens (2002) argued that these earthquake sequences are separated by a high density, mag-

netic body extending to depths of 15 km. They interpreted the composition of this body as a mafic crustal heterogeneity consisting of Jurassic diorite. In contrast, using simple models of fault mechanics, Ron *et al.* (2001) suggested that both Landers and Hector Mine ruptures occurred on both old and young faults in the Mojave. They speculated that old faults were reactivated, which are currently less favorably oriented with respect to the modern regional crustal stress field. So far, the existing seismological data do not make it possible to discern between these two models.

The similarities of the two mainshocks suggest that viscoelastic deformation in the lower crust may provide a possible mechanical coupling (Masterlark and Wang, 2002; Pollitz and Sacks, 2002). Deng et al. (1998) showed that viscoelastic flow in the lower crust was important for explaining the afterslip of the 1992 M_w 7.3 Landers earthquake. Viscoelastic flow beneath a 20-km-thick crust would be consistent with the spacing of the two earthquake ruptures. Similarly, viscoelastic flow beneath the regions east of the Landers rupture would enhance a higher percentage change in strain rate than the region to the west of Landers, due to the decreasing strain from east to west.

The overall tectonic stress field appears to be similar for both earthquakes, although extensional dip-slip faulting is more common for the more northerly Hector Mine aftershocks. Both mainshocks may have caused rotations of the regional stress field. Hauksson (1994) showed that the 1992 M_w 7.3 Landers earthquake rotated the maximum horizontal stress to the east by 7° to 20°. Because of the lower rate of background seismicity, evidence for similar rotations from the Hector Mine mainshock is inconclusive. The possibility of regional stress rotations suggests that the two principal horizontal stresses are of similar size, allowing the stress release of the mainshock to create apparent stress rotations. The implied lack of strong shear stresses further supports the idea of viscoelastic triggering of the Hector Mine earthquake.

Conclusions

The 1999 Hector Mine earthquake sequence was well recorded by the SCSN/TriNet. The background seismicity in the area of the Hector Mine mainshock occurred a few kilometers to the west of the mainshock fault and the immediate foreshocks. The Hector Mine earthquake sequence caused deformation over a wide area, suggesting volumetric shear deformation as opposed to deformation on a single, planar strike-slip fault. The mainshock started on a fault segment with high failure stress and subsequently grew into a larger earthquake by causing slip on fault segments that have low failure stress because they are less favorably oriented to failure. The Hector Mine aftershocks form an asymmetric spatial distribution in which the aftershocks do not center on the main surface break, with most of the aftershocks occurring to the east and north of the surface rupture and in some cases suggesting a steeply dipping fault zone. The Vp and Vp/Vs models show minor small-scale spatial heterogeneities and are similar to the average crustal structure of the Mojave Desert. The *a*-value, a measure of the overall productivity of an aftershock sequence, is the smallest recorded for the three sequences in the ECSZ during the 1990s.

Acknowledgments

Most figures were done using GMT (Wessel and Smith, 1991) and Zmap (Wiemer, 2000). This research was supported by U.S. Geological Survey Grant Numbers 99HQGR0039 and 01HQGR038 to Caltech and grants from the Southern California Earthquake Center. SCEC is funded by NSF Cooperative Agreement Number EAR-8920136 and USGS Cooperative Agreement Numbers 14-08-0001-A0899 and 1434-HQ-97AG01718. SCEC Contribution Number 553. Contribution Number 8748, Division of Geological and Planetary Sciences, California Institute of Technology, Pasadena.

References

Bortugno, E. J., and T. E. Spittler (1986). Geologic map of the San Bernardino quadrangle, California, Map 3A (Geol.), scale 1:250,000 edition, California Division of Mines and Geology, Sacramento.

Deng, J., M. Gurnis, H. Kanamori, and E. Hauksson (1998). Viscoelastic flow in the lower crust after the 1992 Landers, California, earthquake, *Science* **282,** 1689–1692.

Dibblee, T. W., Jr. (1967). Area geology of the western Mojave Desert. *U.S. Geol. Surv. Profess. Pap. 522*, 1–153.

Dokka, R. K., and C. J. Travis (1990a). Late Cenozoic strike-slip faulting in the Mojave Desert, California, *Tectonics* **9,** 311–340.

Dokka, R. K., and C. J. Travis (1990b). Role of the eastern California shear zone in accommodating Pacific–North American plate motion, *Geophys. Res. Lett.* **17,** 1323–1326.

Doser, D. I. (1990). A re-examination of the 1947 Manix, California, earthquake sequence and comparison to other sequences within the Mojave block, *Bull. Seism. Soc. Am.* **80,** 267–277.

Hardebeck, J. L. and E. Hauksson (2001). Crustal stress field in southern California and its implications for fault mechanics, *J. Geophys. Res.* **106,** 21,859–21,882.

Hauksson, E. (1994). State of stress from focal mechanisms before and after the 1992 Landers earthquake sequence, *Bull. Seism. Soc. Am.* **84,** 917–934.

Hauksson, E. (2000). Crustal structure and seismicity distribution adjacent to the Pacific and North America plate boundary in southern California, *J. Geophys. Res.* **105,** 13,875–13,903.

Hauksson, E., L. M. Jones, K. Hutton, and D. Eberhart-Phillips (1993). The 1992 Landers earthquake sequence: seismological observations, *J. Geophys. Res.* **98,** 19,835–19,858.

Jennings, C. W. (1994). Fault map of California with volcanoes, thermal springs and thermal wells, 1:750,000 scale, Geol. Data Map 1, California Division of Mines and Geology, Sacramento.

Ji, C., D. J. Wald, and D. V. Helmberger (2002). Source description of the 1999 Hector Mine, California, earthquake, Part II: Complexity of slip history, *Bull. Seism. Soc. Am.* **92,** 1208–1226 (this issue).

Langenheim, V. E., and R. C. Jachens (2002). The Emerson Lake body: a link between the Landers and Hector Mine earthquakes, southern California, as inferred from gravity and magnetic anomalies, *Bull. Seism. Soc. Am.* **92,** 1606–1620 (this issue).

Masterlark, T. L., and H. F. Wang (2002). Transient stress-coupling between the 1992 Landers and 1999 Hector Mine, California, earthquakes, *Bull. Seism. Soc. Am.* **92,** 1470–1486 (this issue).

McCaffree Pellerin, C. L., and N. I. Christensen, (1998). Interpretation of crustal seismic velocities in the San Gabriel–Mojave region, southern California, *Tectonophysics* **286,** 253–271.

Michael, A. J. (1984). Determination of stress from slip data: faults and folds, *J. Geoph. Res.* **89**, 11,517–11,526.

Parsons, T., and D. S. Dreger (2000). Static-stress impact of the 1992 Landers earthquake sequence on nucleation and slip at the site of the 1999 $M = 7.1$ Hector Mine earthquake, southern California, *Geophys. Res. Lett.* **27,** 1949–1952.

Pollitz, F. F., and I. S. Sacks (2002). Stress triggering of the 1999 Hector Mine earthquake by transient deformation following the 1992 Landers earthquake, *Bull. Seism. Soc. Am.* **92,** 1487–1496 (this issue).

Reasenberg, P. A., and L. M. Jones (1989). Earthquake hazard after a mainshock in California, *Science* **243,** 1173–1175.

Reasenberg, P., and D. Oppenheimer (1985). FPFIT, FPPLOT and FPPAGE: Fortran computer programs for calculating and displaying earthquake fault-plane solutions, *U.S. Geol. Surv. Open-File Rep. 85-739*, 109 pp.

Reyners, M., D. Eberhart-Phillips, and G. Stuart (1999). A three-dimensional image of shallow subduction: crustal structure of the Raukumara Peninsula, New Zealand, *Geophys. J. Int.* **137,** 873–890.

Ron, H., G. Beroza, and A. Nur (2001). Simple models explain complex faulting, *EOS Trans. Am. Geophys. Union* **82,** 125–129.

Sauber, J., W. Thatcher, S. C. Solomon, and M. Lisowski (1994). Geodetic slip rate for the eastern California shear zone and the recurrence time of Mojave Desert earthquakes, *Nature* **367,** 264–266.

Scientists of the U.S. Geological Survey, Southern California Earthquake Center, and California Division of Mines and Geology (2000). Preliminary report on the 16 October 1999 *M* 7.1 Hector Mine, California, earthquake, *Seism. Res. Lett.* **71,** 11–23.

Sieh, K. E., L. M. Jones, E. Hauksson, K. W. Hudnut, D. Eberhart-Phillips, T. H. Heaton, S. E. Hough, L. K. Hutton, H. Kanamori, A. Lilje, S. C. Lindvall, S. F. McGill, J. J. Mori, C. M. Rubin, J. A. Spotila, J. M. Stock, H. K. Thio, J. A. Treiman, B. P. Wernicke, and J. Zachariasen (1993). Near-field investigations of the Landers earthquake sequence, April to July 1992, *Science* **260,** 171–176.

Thurber, C. H. (1993). Local earthquake tomography: velocities and V_P/V_S—theory, in *Seismic Tomography: Theory and Practice*, H. M. Iyer and K. Hirahara (Editors), Chapman and Hall, New York, 563–583.

Treiman, J. A., K. J. Kendrick, W. A. Bryant, T. K. Rockwell, and S. F. McGill (2002). Primary surface rupture associated with the M_w 7.1 16 October 1999 Hector Mine earthquake, San Bernardino County, California, *Bull. Seism. Soc. Am.* **92,** 1171–1191 (this issue).

Unruh, J. R., R. J. Twiss, and E. Hauksson (1996). Seismogenic deformation field in the Mojave block from a micropolar inversion of the 1992 Landers earthquake aftershocks: implications for tectonics of the eastern California shear zone, *J. Geophys. Res.* **101,** 8335–8361.

Waldhauser, F., and W. L. Ellsworth (2000). A double-difference earthquake location algorithm: method and application to the northern Hayward fault, California, *Bull. Seism. Soc. Am.* **90,** 1353–1368.

Wessel, P., and W. H. F. Smith (1991). Free software helps map and display data, *EOS Trans. Am. Geophys. Union* **72,** 441, 445–446.

Wiemer, S. (2000). The seismicity analysis software, ZMAP, *http://www.seismo.ethz.ch*.

Wiemer, S., M. Gerstenberger, and E. Hauksson (2002). Properties of the aftershock sequence of the 1999 M_w 7.1 Hector Mine earthquake: implications for aftershock hazard, *Bull. Seism. Soc. Am.* **92,** 1227–1240 (this issue).

Zhao, D., H. Kanamori, H. Negishi, and D. Wiens (1996). Tomography of the source area of the 1995 Kobe earthquake: evidence for fluids at the hypocenter?, *Science* **274,** 1891–1894.

California Institute of Technology, Seismological Laboratory
Mail Code 252-21
1200 E. California Blvd.
Pasadena, California 91125
(E.H., K.H.)

U.S. Geological Survey
535 S. Wilson Ave.
Pasadena, California 91106
(L.M.J.)

Manuscript received 10 December 2000.